Published in final edited form as:
Med Phys. 2007 February ; 34(2): 564–576.

Scatter radiation in digital tomosynthesis of the breast

Ioannis Sechopoulos,
Department of Radiology and Winship Cancer Institute, Emory University School of Medicine, 1701 Uppergate Drive, Suite 5018, Atlanta, Georgia 30322 and Wallace H. Coulter Department of Biomedical Engineering, Georgia Institute of Technology, 313 Ferst Drive, Atlanta, Georgia 30332

Sankararaman Suryanarayanan,
Department of Radiology and Winship Cancer Institute, Emory University School of Medicine, 1701 Uppergate Drive, Suite 5018, Atlanta, Georgia 30322

Srinivasan Vedantham,
Department of Radiology and Winship Cancer Institute, Emory University School of Medicine, 1701 Uppergate Drive, Suite 5018, Atlanta, Georgia 30322

Carl J. D'Orsi, and
Department of Radiology and Winship Cancer Institute, Emory University School of Medicine, 1701 Uppergate Drive, Suite 5018, Atlanta, Georgia 30322

Andrew Karellas[a]
Department of Radiology and Winship Cancer Institute, Emory University School of Medicine, 1701 Uppergate Drive, Suite 5018, Atlanta, Georgia 30322 and Wallace H. Coulter Department of Biomedical Engineering, Georgia Institute of Technology, 313 Ferst Drive, Atlanta, Georgia 30332

Abstract

Digital tomosynthesis of the breast is being investigated as one possible solution to the problem of tissue superposition present in planar mammography. This imaging technique presents various advantages that would make it a feasible replacement for planar mammography, among them similar, if not lower, radiation glandular dose to the breast; implementation on conventional digital mammography technology via relatively simple modifications; and fast acquisition time. One significant problem that tomosynthesis of the breast must overcome, however, is the reduction of x-ray scatter inclusion in the projection images. In tomosynthesis, due to the projection geometry and radiation dose considerations, the use of an antiscatter grid presents several challenges. Therefore, the use of postacquisition software-based scatter reduction algorithms seems well justified, requiring a comprehensive evaluation of x-ray scatter content in the tomosynthesis projections. This study aims to gain insight into the behavior of x-ray scatter in tomosynthesis by characterizing the scatter point spread functions (PSFs) and the scatter to primary ratio (SPR) maps found in tomosynthesis of the breast. This characterization was performed using Monte Carlo simulations, based on the Geant4 toolkit, that simulate the conditions present in a digital tomosynthesis system, including the simulation of the compressed breast in both the cranio-caudal (CC) and the medio-lateral oblique (MLO) views. The variation of the scatter PSF with varying

[a]Author to whom correspondence should be addressed. Electronic mail: akarell@emory.edu.

tomosynthesis projection angle, as well as the effects of varying breast glandular fraction and x-ray spectrum, was analyzed. The behavior of the SPR for different projection angle, breast size, thickness, glandular fraction, and x-ray spectrum was also analyzed, and computer fit equations for the magnitude of the SPR at the center of mass for both the CC and the MLO views were found. Within mammographic energies, the x-ray spectrum was found to have no appreciable effect on the scatter PSF and on the SPR. Glandular fraction and compressed breast size were found to have a small effect, while compressed breast thickness and projection angle, as expected, introduced large variations in both the scatter PSF and SPR. The presence of the breast support plate and the detector cover plate in the simulations introduced important effects on the SPR, which are also relevant to the scatter content in planar mammography.

Keywords

tomosynthesis; digital mammography; scatter; breast; Monte Carlo

I. INTRODUCTION

While the introduction of screening mammography has been responsible for an important reduction in breast cancer mortality, 1 conventional (planar) mammography has certain limitations. One of the major limitations inherent to planar mammography is the representation of three-dimensional information in a two-dimensional image, which inevitably introduces tissue superposition. This effect is one of the major factors for false positives2,3 and may alone be responsible for about 25% of all mammography recalls.4 To overcome this limitation, extensive research is in progress to introduce new imaging techniques that present at least some depth information to the radiologist. One of these new imaging techniques is digital tomosynthesis of the breast, which involves acquiring a set of radiographic projections over a limited angular range and combining these projections to reconstruct a quasi-three-dimensional image.5–9 A different approach, dedicated breast computed tomography, aims at acquiring cone beam projections of the breast that result in a 3D reconstruction of the breast volume.10–13

In one of the variations of digital tomosynthesis imaging of the breast, the x-ray tube rotates through a limited angular range around the compressed breast, while the breast and the digital imager remain stationary (Fig. 1).14,15 The movement of the x-ray tube with respect to the digital imager during acquisition of the tomosynthesis projections makes the use of an antiscatter grid challenging. With the use of a traditional linear or cellular antiscatter grid, the primary (nonscattered) x rays incident on the imager for the oblique views would be cut off. At a tomosynthesis projection angle of 10°, approximately 65% and 88% of the primary x rays would be cut off at the center of the detector by antiscatter grids with grid ratios of 4:1 and 5:1,16 while at 15° and 11°, respectively, all primary x rays would be cut off. A focused linear antiscatter grid with the septa oriented parallel to the chest wall could be used if the motion mechanism of the grid is also reoriented. Other options to make antiscatter grids suitable in tomosynthesis imaging are to have a low grid ratio with inefficient scatter rejection or to rotate the septa of the grid with the x-ray tube to maintain their parallelism with the incident x rays for all projections. All these variations would still suffer from the

limitation that antiscatter grids do not absorb all incident scattered x rays and do not transmit all incident primary x rays, 17 and therefore other methods for scatter rejection are being sought. A different approach that is being investigated for the reduction of x-ray scatter content in the projections is to introduce postacquisition, software-based scatter reduction. 18–22 Several scatter reduction algorithms have been proposed for planar mammography and could be potentially adapted for digital tomosynthesis. However, all scatter reduction algorithms require some form of prior knowledge of the scatter content in the images to be processed. This prior knowledge includes the scatter point spread function (PSF) or the scatter to primary ratio (SPR).

The purpose of this study is to characterize x-ray scatter in digital tomosynthesis of the breast to facilitate the further development and application of software-based scatter reduction techniques to tomosynthesis projection images. Extensive studies based on experimental and simulation methods have been published on x-ray scatter in planar mammography20,23–29 and some work has been done on characterizing x-ray scatter in breast CT.30 Although limited studies of x-ray scatter in breast tomosynthesis have been presented, 21,31–33 no comprehensive characterization of the x-ray scatter in tomosynthesis projections of clinically realistic mammographic shapes has been reported. In this work, the variation of x-ray scatter content in the tomosynthesis projections under different conditions such as varying breast size, compressed thickness, composition, x-ray spectrum, and tomosynthesis projection angle is studied. Computer fit equations for the SPR at the center of mass, as well as insights into the variations in scatter PSF with varying projection angle, are reported.

II. METHODS AND MATERIALS

A. Monte Carlo simulation software

A previously developed Monte Carlo based simulation program that models image acquisition during a tomosynthesis of the breast examination was used for this study.34 This C++ based program, based on the Geant4 toolkit, 35,36 models the compressed breast in both the craniocaudal (CC) and the medio-lateral oblique (MLO) views (Fig. 2) and includes the imaging system's compression plate, support plate, detector cover plate, an ideal energy integrating detector, and the patient's body. The compression plate was modeled as polycarbonate with a thickness of 2 mm, while the combination of the breast support plate and cover plate was equivalent to 3.3 mm of carbon fiber. The patient's body was included to take backscatter into account and was modeled as a very large volume of water. The x-ray tube is simulated as a point source, 66 cm above the detector at the 0° projection angle, which rotates around the compressed breast according to the tomosynthesis projection angle and the location of the rotation center (4 cm above the detector) of the x-ray tube. It was assumed that the collimation varied with projection angle so that the x-ray field is restricted to illuminate the detector area completely from any position. The x-ray field simulation also includes the heel effect and the inverse square distance relationship, introducing a falloff in intensity away from the central ray. The detector was modified so that it can discriminate between primary (x rays that did not undergo any scatter event) and scatter (x rays that underwent at least one scatter event) photons. This results in two separate images being

recorded per acquisition, one primary and one scatter image. The simulated detector was programmed to have a 1 mm resolution, which was deemed small enough for appropriate characterization of x-ray scatter variation with position, but still large enough to obtain reasonable statistics. This resulted in SPR maps of size 240×307.

B. Characterization of scatter to primary ratio

To analyze how the SPR varies under different conditions, the Monte Carlo simulation was performed repeatedly while varying breast size, specified as the chest wall to nipple distance (CND) and compressed breast thickness (*T*), for both CC and MLO views. Simulations were performed for the compressed breast using a 50% glandular fraction, as described by Hammerstein *et al.*37 with the CND and *T* set to the values specified in Table I. For the compressed breast in CC view, the CND was chosen so that the breast tissue mass would be equal to that of the MLO simulations, not including the pectoralis muscle. To study the behavior of SPR with glandular fraction, additional simulations were performed by setting the glandular fraction to 0%, 25%, 50%, 75%, and 100% for the more limited set of parameter values shown in the second part of Table I.

For each breast setup, projections were acquired at ±30° in 6° steps (due to symmetry, only the positive angles were used for the CC view studies). For each of these 518 geometry and composition combinations, 50 million monochromatic x rays at each energy between 9.5 and 31.5 keV in steps of 1 keV were tracked. This resulted in a total of 11 914 sets of primary and scatter images. To perform these simulations, a 64 node computer cluster, each node containing two AMD Opteron 2.2 GHz processors (Advanced Micro Devices, Inc., Sunnyvale, CA), was used. To obtain SPR maps for a specified x-ray spectrum, the monochromatic primary and scatter images were median filtered (11×11 kernel size) to reduce noise, weighted by the relative number of photons at each energy bin of the spectrum, and then totaled to obtain spectrum-weighted primary and scatter images. A median filter, rather than a mean filter, was used because it was found by analyzing pre- and post-filter profiles of the data that, although the noise reduction was similar, the median filter preserved the sharp features present in the primary images better than the mean filter. The spectrum-weighted spatially variant SPR maps were obtained by pixel-by-pixel division of the spectrum-weighted scatter image by the spectrum-weighted primary image. To study how the x-ray spectrum affects the SPR, the monochromatic data were combined using the relative number of photons for seven different spectra, 38 specified in Table II. From these simulations, the SPR at the projection of the center of mass (COM) of the breast was found and its variation under the different imaging conditions characterized. The SPR at the center of mass reported is the mean from a 1×1 cm region surrounding the COM. In addition, SPR maps and profiles are presented for qualitative analysis.

C. Study of scatter point spread functions

Scatter reduction algorithms typically require an estimate of the scatter PSF as prior knowledge. To gain insight into how the scatter PSF behaves in tomosynthesis conditions, the Monte Carlo simulation was modified so that the x-ray field was reduced to a pencil beam directed at the center of mass. The variation in shape of the scatter PSF for different projection angles is presented. This analysis was performed only for a breast in the CC view

with CND=10 cm, T=2, 5, and 8 cm, G=0%, 50%, and 100%, and projection angles from 0° to 30° in 6° steps.

To reduce computation time, a variance reduction scheme, based on the concept of importance sampling, 39 was introduced in the Geant4 simulation. This scheme consisted of modifying the Rayleigh and Compton scatter physics models so that at each scatter event, more than one photon would be output, each one sampled independently from the appropriate energy and angular distribution functions for the incident photon. To compensate for this multiplication of photons, a relative weight was assigned to each photon, so that each original photon emitted from the x-ray source had a weight value of 1, and this value was reduced according to the number of photons that were produced for each scatter event. For example, if, at each scatter event, the incident photon were split into five photons, these output photons would each have a relative weight of 0.2. If any of these photons scattered again, another five photons would be produced, each one with a relative weight of 0.04. When a photon arrived at the imager, the number recorded at that position would be the photon energy times its relative weight. To verify that this variance reduction scheme yielded the correct results, the same simulation was repeated with and without the variance reduction. The resulting PSFs for both cases were virtually identical and are shown in Fig. 3. This variance reduction scheme succeeded in reducing the number of emitted x rays needed to be simulated, since the computer program spends more processing time following the x rays that have scattered and less time following the primary x rays that do not provide scatter information.

D. Validation

Although the Geant4 Monte Carlo toolkit has been already validated for x-ray scatter studies at mammographic energies, 40 and our Geant4 tomosynthesis simulator was validated for glandular radiation dose predictions, 34 our program was modified to match the geometry described by Boone and Cooper, 24 to compare Geant4's predictions on scatter PSF for the 0° projection angle with the scatter PSF reported for planar mammography.

III. RESULTS

To verify the statistical precision obtained by performing monochromatic runs of 50 million photons, two simulations were repeated five times to compute the coefficient of variation (defined as the percentage ratio of standard deviation to the mean, COV=100σ/μ) of the SPR at the COM. For an average breast, 5 cm thick, CND=11.6 cm, G=50%, projection angle=0°, the COV for the spectra below 27 kVp was lower than 1.25%, while for the rest the COV was 0.5% or lower. For a similar breast but with the maximum thickness, 8 cm, the COV for the Mo/Mo 25 kVp spectrum was 8.6%, while for the 27 kVp spectra the COV was lower than 5.0%, and for the 29 kVp spectra and above the COV fell to below 1.8%. Considering that in a clinical environment an 8 cm thick compressed breast is rarely imaged with a spectrum below 27 kVp, this precision was deemed sufficient.

A. Validation

Figure 4 shows the scatter PSFs computed by the Geant4 simulation compared to those reported by Boone and Cooper.24 The scatter PSFs presented are radially averaged and normalized to the number of primary photons detected. The results show agreement for all the variations reported by Boone and Cooper, which included varying breast tissue composition, x-ray spectrum, breast-to-imager air gap, and compressed breast thickness.

B. Qualitative analysis of the scatter point spread function

Figure 5 shows images of the computed scatter PSF for a 5 cm thick compressed breast, 50% glandular fraction and tomosynthesis projection angles ranging from 0° to 30° in 6° steps. The radial symmetry of the 0° scatter PSF is clear. Some progressive loss of symmetry can be observed with increased angle, with the last two projection angles (24° and 30°) presenting an obvious asymmetry. In these images, the x-ray tube moves toward the top of the page with increasing projection angle. This shows that as the x-ray tube moves in one direction, the "tail" of the scatter PSF is extended towards the opposite direction.

Vertical profiles through the center of the scatter PSF for the three different compressed breast thicknesses simulated are shown in Fig. 6. The x-ray tube moves towards the negative side of the *x* axis with increasing projection angle. The increase in scatter in the direction opposite to tube movement, resulting in an asymmetric PSF, can be seen. This effect becomes more pronounced with increasing compressed breast thickness. It is important to note that asymmetry can be already seen at the 6° projection angle, which was not apparent in the two-dimensional images.

The effect of glandular fraction and x-ray spectra on the behavior of the scatter PSF with angle is depicted in Fig. 7. In both cases, as expected, a very small deviation was found.

C. Effect of the breast support plate and detector cover plate on the scatter to primary ratio

Figure 8 shows the computed SPR maps for compressed breasts of varying thickness in the CC view for the 0° and 30° tomosynthesis projection angles. The simulated breasts have a CND=11.6 cm, T=2, 5, and 8 cm, and G=50%, and the x-ray spectrum is Rh/Rh 31 kVp. Figure 9 shows the same cases in the MLO view, but with a CND=13 cm. The images for the 5 and 8 cm thick breasts present a sharp increase in the SPR close to the outer edges of the compressed breast. This increase in SPR, although to a lesser degree, was previously reported by Lam and Chan.41 To isolate the cause of these spikes in the SPR maps, three different modifications to the CC view simulations were attempted. In the first case, the possibility that this effect is due to the drop-off in tissue thickness at the curved edge of the compressed breast was studied by modifying the breast to be a perfect cylinder with semi-circular cross section. To study the possibility that the inclusion of a 4 mm skin layer around the breast introduced unexpected differences in scattering cross sections, the skin layer was eliminated in a second simulation. With these two variations, the spike in the SPR profile was still present.

The third modification of the simulation eliminated the breast compression plate, breast support plate, and detector cover plate. The results of this simulation are shown in Figs. 10 and 11, where it is clear that this effect did not occur. Figures 12 and 13 show horizontal (perpendicular to the x-ray tube's motion) profiles through the projection of the center of mass of the compressed breast showing clearly the effect that the presence of these plates has on the SPR. The spike and overall increase in SPR is due to the scattering contribution of the open field area of the plates. Although the plates are very thin compared to the compressed breast, the sections of these plates outside the area of the compressed breast are exposed to the full fluence of the x-ray field, causing the absolute number of x rays detected that underwent a scattering event in the open area of the plates to be high. Some portion of the x rays that scattered in the plates is detected under the shadow of the breast, where the number of primary x rays detected is reduced substantially due to the attenuation of the breast. This phenomenon is depicted graphically in Fig. 14. The reduced attenuation of the primary x rays in the thin breasts explains why this effect is not seen as prominently in the SPR maps for breast of T=2 cm.

The rest of the SPR results reported in this paper are from simulations that include the breast compression plate, breast support plate, and detector cover plate, since these are always necessarily present during a clinical tomosynthesis acquisition.

D. Scatter to primary ratio maps

Figure 15 shows the 3D plot of the SPR maps of a compressed breast in the CC view (CND=11.6 cm, T=5 cm, G =50%, Rh/Rh 31kVp) for projection angles 0° to 30° in 6° steps. As in the scatter PSF section, the x-ray tube's movement with increasing projection angle is towards the negative side of the x axis. The increase in SPR throughout the breast with increasing projection angle can be clearly seen. In addition, the symmetry of the SPR about the centerline of the imager is lost, with the tail of the SPR on the side opposite the x-ray tube becoming wider. This effect is expected, if one considers the shape of the scatter PSF described in the previous section. The increased SPR around the edge of the breast because of the presence of the compression plate, support plate, and cover plate can also be seen, especially in the wider angle projection images. For improved visibility, profiles parallel to the chest wall (also parallel to the x-ray tube's motion), through the center of mass, are depicted in Fig. 16. Profiles for compressed breasts of thickness 2 and 5 cm are also shown. The overall increase in SPR, loss of asymmetry, and the higher SPR at the borders can all be also seen in the profiles. In addition, the increase in SPR close to the borders of the breast can be seen more prominently for the T=8 cm breast.

E. Scatter to primary ratio at the center of mass

Figures 17 and 18 show the variation of the SPR at the center of mass with varying breast size, thickness composition, and x-ray spectrum for the CC and MLO views, respectively. Unless specified otherwise, the data shown are for a breast with CND=13 cm (11.6 cm for the CC view), T =5 cm, G=50%, and Rh/Rh 31 kVp x-ray spectrum. As expected, SPR is most of all a function of compressed breast thickness, with a smaller dependence on glandularity and breast size. Specifically, chest wall to nipple distance appears to only have an influence on SPR when it is below a certain value. These results are consistent with those

reported by Boone *et al.*,25 in which the SPR curve approaches a horizontal line with increasing breast size and can be explained by the falloff in intensity of the scatter PSF with radial distance. The x-ray spectrum does not appear to influence the SPR; the few data points that show some deviation can probably be attributed to higher statistical noise due to the fact that those points are the ones that include the fewest total x-ray histories.

Given these results, the computed data were used to fit an equation for SPR as a function of tomosynthesis projection angle, compressed breast thickness, and breast glandularity for each view. This was accomplished using commercially available software (TableCurve 3D and TableCurve 2D, Systat Software Inc., Richmond, CA). Since TableCurve 3D can only fit functions with two independent variables, the glandularity dependence was introduced as a linear coefficient to the surface equation found by TableCurve 3D for SPR(T, α). The resulting equations for scatter to primary ratio at the center of mass for a tomosynthesis projection were as follows:

For MLO view,

$$\mathrm{SPR}_{\mathrm{MLO}}=(aG+b)\frac{(c+dT+e\alpha+fT^2+g\alpha^2+hT\alpha)}{(1+iT+j\alpha+kT^2+l\alpha^2+mT\alpha)}. \quad (1)$$

For CC view,

$$\mathrm{SPR}_{\mathrm{CC}}=(aG+b)\frac{(c+dT+eT^2+fT^3+g\alpha)}{(1+hT+i\alpha+j\alpha^2+kT\alpha^3)}. \quad (2)$$

where α is the tomosynthesis angle (measured from the detector surface),34 in degrees; T is the compressed breast thickness, in cm; and a through m are the fit coefficients, given in Table III. Both fits resulted in a R^2>0.976 and are applicable for any chest wall to nipple distance above 10 cm in MLO view, and for any CND for CC view.

IV. DISCUSSION

The variation found in the scatter point spread functions with varying tomosynthesis projection angle suggests the need of using different scatter PSFs when attempting to perform scatter reduction image processing on tomosynthesis projections. Assuming the same scatter PSF for all projections would clearly result in suboptimal corrections. To obtain estimations of the scatter PSF of a real breast, a Monte Carlo program like the one described in this study, which assumes a homogeneous breast, is appropriate given the small variation in PSF for breasts with different glandular fractions. In addition, the same simulated scatter PSF can be used for a breast imaged with different x-ray spectra, given the very small variation found within mammographic energies. To compute the scatter PSF using Monte Carlo simulations, a variance reduction scheme like the one included in this work may be used, allowing for an important reduction in computation time.

If the scatter reduction technique being used involves an estimation of the SPR map as prior knowledge, it is important to compute the map with the presence of the breast support plate

and detector cover plate included in the Monte Carlo simulation. As seen in the results, these contribute a very important amount of scatter close to the breast edge portion of the image, and in general increase the SPR throughout the whole breast. Using Boone *et al.*'s equation for SPR at the center of mass for a semi-circular breast in planar mammography, 25 the SPRs for the CND=11.6 cm, T=2, 5, and 8 cm breast should be 0.24, 0.55, and 1.03, respectively. In our simulations, the values found when no plates are present were 0.26, 0.57, and 0.91 for the same three conditions. With the plates present, these values increase to 0.34, 0.67, and 1.03. This comparison not only serves as validation for our simulations, but shows that if the plates are not taken into account, the SPR estimation in an image may be underestimated by as much as 31%.

By performing the same simulation for varying values of the four parameters relevant to the simulation, compressed breast thickness, breast size, glandular fraction, and x-ray spectrum, it was found that the SPR is, as expected, largely a function of thickness and, to a small extent, glandular fraction. The x-ray spectrum used, within mammographic energies, did not show any real variation in SPR. The breast size seems to affect SPR in very small breasts; when CND is past a certain threshold the SPR increase becomes very slow. This is expected due to the scatter PSF's limited range. Given these variations, equations were fit to be able to compute the SPR at the center of mass for a breast of any thickness between 2 and 8 cm, glandular fraction between 0% and 100%, and for any tomosynthesis projection angle between ±30°.

Although in a clinical image an imaged breast will present anatomical structure, and is therefore not homogeneous, the small variations found in the scatter PSF and in the SPR maps for homogeneous breasts of varying glandular fraction seem to suggest that Monte Carlo simulations are still useful for the development of scatter reduction algorithms for application in clinical images.

Two other sources of resolution and contrast loss that are present in a clinical system but were ignored in this study are off-focus radiation and detector response. By excluding off-focus radiation from the simulation, the results presented are applicable independent of the x-ray tube used, and this effect can be added to the x-ray scatter effect described here. In addition, it has been shown that for the spectral energies analyzed in this study, the off-focus radiation-to-primary ratio varies approximately from 0.035 to 0.045,42 which is approximately 3% to 10% of the scatter to primary ratio found in this study, depending on the breast thickness.

The nonideal detector response was excluded due to the vast variety of parameters (x-ray, optical, or electron spatial spread, conversion media thickness, packing fraction, columnar structure, etc.) that would have to be encompassed to make a comprehensive analysis. These effects have been studied for various imager technologies and incidence angles43–45 and can be combined with the effects described in this study for any specific system.

In this study we assumed that the heel effect causes the same drop-off in intensity for x rays of all energies. The validity of this assumption was checked by computing the first half value layer (HVL) of the spectrum reaching the detector along the central ray (therefore

exiting the anode straight down and entering the added filtration orthogonally) and of the spectrum reaching the detector at the farthest corner (therefore traveling through a longer path in the anode and the added filtration). The increase in HVL for the lowest energy spectrum used in this study (Mo/Mo 25 kVp) was found to be approximately 16%, while for the highest energy spectrum (Rh/Rh 31 kVp) was computed to be approximately 11%. Given the SPR's very weak dependence on x-ray spectrum, it is estimated that this difference is negligible.

Similar simulations for the study of scatter PSF and SPR, even with the presence of an antiscatter grid, in the emerging field of dedicated cone beam breast computed tomography might prove useful, given the potential for introduction of artifacts in the reconstructed volume due to the inclusion of scatter in the projection images.

V. CONCLUSION

X-ray scatter inclusion in the image is an important concern in all radiographic applications. In digital tomosynthesis of the breast, x-ray scatter is an especially important consideration due to the difficulty of the use of an antiscatter grid. To reduce the deleterious effect of x-ray scatter in the tomosynthesis projections, the use of postacquisition software-based x-ray scatter reduction techniques is being investigated.21,31 This necessitates a comprehensive understanding of the x-ray scatter content in the tomosynthesis projections. In this study, insight has been obtained as to the behavior of x-ray scatter in a tomosynthesis projection with varying projection angle. By analyzing the scatter point spread function and the scatter to primary ratio map for different conditions, the importance of considering the projection angle when attempting to reduce the scatter content of an image was identified.

The magnitude of the effect on the SPR due to the presence of the breast support plate and the detector cover plate was found to be higher than expected. This effect impacts not only tomosynthesis imaging, but planar mammography as well.

Acknowledgments

The authors would like to thank Steve Pittard for providing technical assistance with the use of Emory University's High Performance Computer Cluster. This study was supported in part by the National Institutes of Health (NIH) Grant No. RO1-EB002123 from the National Institute of Biomedical Imaging and Bioengineering (NIBIB). This work was also supported by a grant from the Georgia Cancer Coalition (GCC). The contents are solely the responsibility of the authors and do not necessarily represent the official views of the NIH, NIBIB, or the GCC.

References

1. Humphrey LL, Helfand M, Chan BK, Woolf SH. Breast cancer screening: a summary of the evidence for the U.S. Preventive Services Task Force. Ann Intern Med. 2002; 137:347–360. [PubMed: 12204020]
2. Tabar L, Fagerberg G, Chen HH, Duffy SW, Smart CR, Gad A, Smith RA. Efficacy of breast cancer screening by age. New results from the Swedish two-county trial. Cancer. 1995; 75:2507–2517. [PubMed: 7736395]
3. Rosenberg RD, Lando JF, Hunt WC, Darling RR, Williamson MR, Linver MN, Gilliland FD, Key CR. The New Mexico mammography project: Screening mammography performance in Albuquerque, New Mexico, 1991 to 1993. Cancer. 1996; 78:1731–1739. [PubMed: 8859186]

4. Kopans DB. Beyond randomized controlled trials: organized mammographic screening substantially reduces breast carcinoma mortality. Cancer. 2002; 94:580–581. 94, 581–583, (2002). [PubMed: 11900247]
5. Niklason LT, et al. Digital tomosynthesis in breast imaging. Radiology. 1997; 205:399–406. [PubMed: 9356620]
6. Kolitsi Z, Panayiotakis G, Anastassopoulos V, Scodras A, Pallikarakis N. A multiple projection method for digital tomosynthesis. Med Phys. 1992; 19:1045–1050. [PubMed: 1518466]
7. Dobbins JT III, Godfrey DJ. Digital x-ray tomosynthesis: current state of the art and clinical potential. Phys Med Biol. 2003; 48:R65–R106. [PubMed: 14579853]
8. Suryanarayanan S, Karellas A, Vedantham S, Baker SP, Glick SJ, D'Orsi CJ, Webber RL. Evaluation of linear and nonlinear tomosynthetic reconstruction methods in digital mammography. Acad Radiol. 2001; 8:219–224. [PubMed: 11249085]
9. Suryanarayanan S, Karellas A, Vedantham S, Glick SJ, D'Orsi CJ, Baker SP, Webber RL. Comparison of tomosynthesis methods used with digital mammography. Acad Radiol. 2000; 7:1085–1097. [PubMed: 11131053]
10. Boone JM, Nelson TR, Lindfors KK, Seibert JA. Dedicated breast CT: radiation dose and image quality evaluation. Radiology. 2001; 221:657–667. [PubMed: 11719660]
11. Zeng K, Yu H, Fajardo LL, Wang G. Cone-beam mammo-computed tomography from data along two tilting arcs. Med Phys. 2006; 33:3621–3633. [PubMed: 17089827]
12. Ning R, Conover DL, Chen B, Schiffhauer L, Cullinan J, Ning Y, Robinson AE. Flat-panel-detector-based cone-beam volume CT breast imaging: phantom and specimen study. Proc SPIE. 2002; 4682:218–227.
13. Ning R, Yu Y, Conover DL, Lu X, He H, Chen Z, Schiffhauer L, Cullinan J. Preliminary system characterization of flat-panel-detector-based cone-beam CT for breast imaging. Proc SPIE. 2004; 5368:292–303.
14. Eberhard JW, et al. High-speed large-angle mammography tomosynthesis system. Proc SPIE. 2006; 6142:61420C–61411C.
15. Wu T, et al. Tomographic mammography using a limited number of low-dose cone-beam projection images. Med Phys. 2003; 30:365–380. [PubMed: 12674237]
16. Rezentes PS, de Almeida A, Barnes GT. Mammography grid performance. Radiology. 1999; 210:227–232. [PubMed: 9885613]
17. Kaufhold J, Thomas JA, Eberhard JW, Galbo CE, Trotter DEG. A calibration approach to glandular tissue composition estimation in digital mammography. Med Phys. 2002; 29:1867–1880. [PubMed: 12201434]
18. Baydush AH, Floyd CE Jr. Improved image quality in digital mammography with image processing. Med Phys. 2000; 27:1503–1508. [PubMed: 10947253]
19. Gonzalez Trotter DE, Tkaczyk JE, Kaufhold J, Claus BEH, Eberhard JW. Thickness-dependent scatter correction algorithm for digital mammography. Proc SPIE. 2002; 4682:469–478.
20. Nykanen K, Siltanen S. X-ray scattering in full-field digital mammography. Med Phys. 2003; 30:1864–1873. [PubMed: 12906205]
21. Sechopoulos I, Suryanarayanan S, Vedantham S, Karellas A. SU-FF-I-35: Scatter correction for digital tomosynthesis. Med Phys. 2005; 32:1911–1912.
22. Seibert JA, Boone JM. X-ray scatter removal by deconvolution. Med Phys. 1988; 15:567–575. [PubMed: 3211049]
23. Barnes GT, Brezovich IA. The intensity of scattered radiation in mammography. Radiology. 1978; 126:243–247. [PubMed: 619418]
24. Boone JM, Cooper VN III. Scatter/primary in mammography: Monte Carlo validation. Med Phys. 2000; 27:1818–1831. [PubMed: 10984229]
25. Boone JM, Lindfors KK, Cooper VN III, Seibert JA. Scatter/primary in mammography: comprehensive results. Med Phys. 2000; 27:2408–2416. [PubMed: 11099211]
26. Cooper VN III, Boone JM, Seibert JA, Pellot-Barakat CJ. An edge spread technique for measurement of the scatter-to-primary ratio in mammography. Med Phys. 2000; 27:845–853. [PubMed: 10841386]

27. Dance DR, Day GJ. The computation of scatter in mammography by Monte Carlo methods. Phys Med Biol. 1984; 29:237–247. [PubMed: 6709703]
28. Fritz SL, Chang CH, Livingston WH. Scatter/primary ratios for x-ray spectra modified to enhance iodine contrast in screen-film mammography. Med Phys. 1983; 10:866–870. [PubMed: 6656696]
29. Klein DJ, Chan HP, Muntz EP, Doi K, Lee K, Chopelas P, Bernstein H, Lee J. Experimental and theoretical energy and angular dependencies of scattered radiation in the mammography energy range. Med Phys. 1983; 10:664–668. [PubMed: 6646072]
30. Kwan ALC, Boone JM, Shah N. Evaluation of x-ray scatter properties in a dedicated cone-beam breast CT scanner. Med Phys. 2005; 32:2967–2975. [PubMed: 16266111]
31. Liu B, Wu T, Moore RH, Kopans DB. Monte Carlo simulation of x-ray scatter based on patient model from digital breast tomosynthesis. Proc SPIE. 2006; 6142:61421N–61429N.
32. Liu B, Glick S, Gong X. TU-EE-A3-05: Scatter radiation in digital tomosynthesis. Med Phys. 2005; 32:2105–2105.
33. Karellas, A. Radiological Society of North America Scientific Assembly and Annual Meeting Program. Radiological Society of North America; Oak Brook, IL: 2006. Digital mammography image acquisition technology; p. 148
34. Sechopoulos I, Suryanarayanan S, Vedantham S, D'Orsi C, Karellas A. Computation of the glandular radiation dose in digital tomosynthesis of the breast. Med Phys. 2007; 34:221–232. [PubMed: 17278508]
35. Agostinelli S, et al. Geant4—a simulation toolkit. Nucl Instrum Methods Phys Res A. 2003; 506:250–303.
36. Allison J, et al. Geant4 developments and applications. IEEE Trans Nucl Sci. 2006; 53:270–278.
37. Hammerstein GR, Miller DW, White DR, Masterson ME, Woodard HQ, Laughlin JS. Absorbed radiation dose in mammography. Radiology. 1979; 130:485–491. [PubMed: 760167]
38. Boone JM, Fewell TR, Jennings RJ. Molybdenum, rhodium, and tungsten anode spectral models using interpolating polynomials with application to mammography. Med Phys. 1997; 24:1863–1874. [PubMed: 9434969]
39. Hammersley, JM.; Handscomb, DC. Monte Carlo Methods. Methuen, Wiley; London: 1964.
40. Grabski V, Brandan ME, Ruiz-Trejo C, Villasenor Y. SU-FF-I-34: PSF and S/P in mammography: A validation of simulations using the GEANT4 Code. Med Phys. 2005; 32:1911–1911.
41. Lam KL, Chan HP. Effects of x-ray beam equalization on mammographic imaging. Med Phys. 1990; 17:242–249. [PubMed: 2333050]
42. Shen SZ, Bloomquist AK, Mawdsley GE, Yaffe MJ, Elbakri I. Effect of scatter and an antiscatter grid on the performance of a slot-scanning digital mammography system. Med Phys. 2006; 33:1108–1115. [PubMed: 16696488]
43. Mainprize JG, Bloomquist AK, Kempston MP, Yaffe MJ. Resolution at oblique incidence angles of a flat panel imager for breast tomosynthesis. Med Phys. 2006; 33:3159–3164. [PubMed: 17022208]
44. Vedantham S, et al. Full breast digital mammography with an amorphous silicon-based flat panel detector: physical characteristics of a clinical prototype. Med Phys. 2000; 27:558–567. [PubMed: 10757607]
45. Que W, Rowlands JA. X-ray imaging using amorphous selenium: Inherent spatial resolution. Med Phys. 1995; 22:365–374. [PubMed: 7609716]

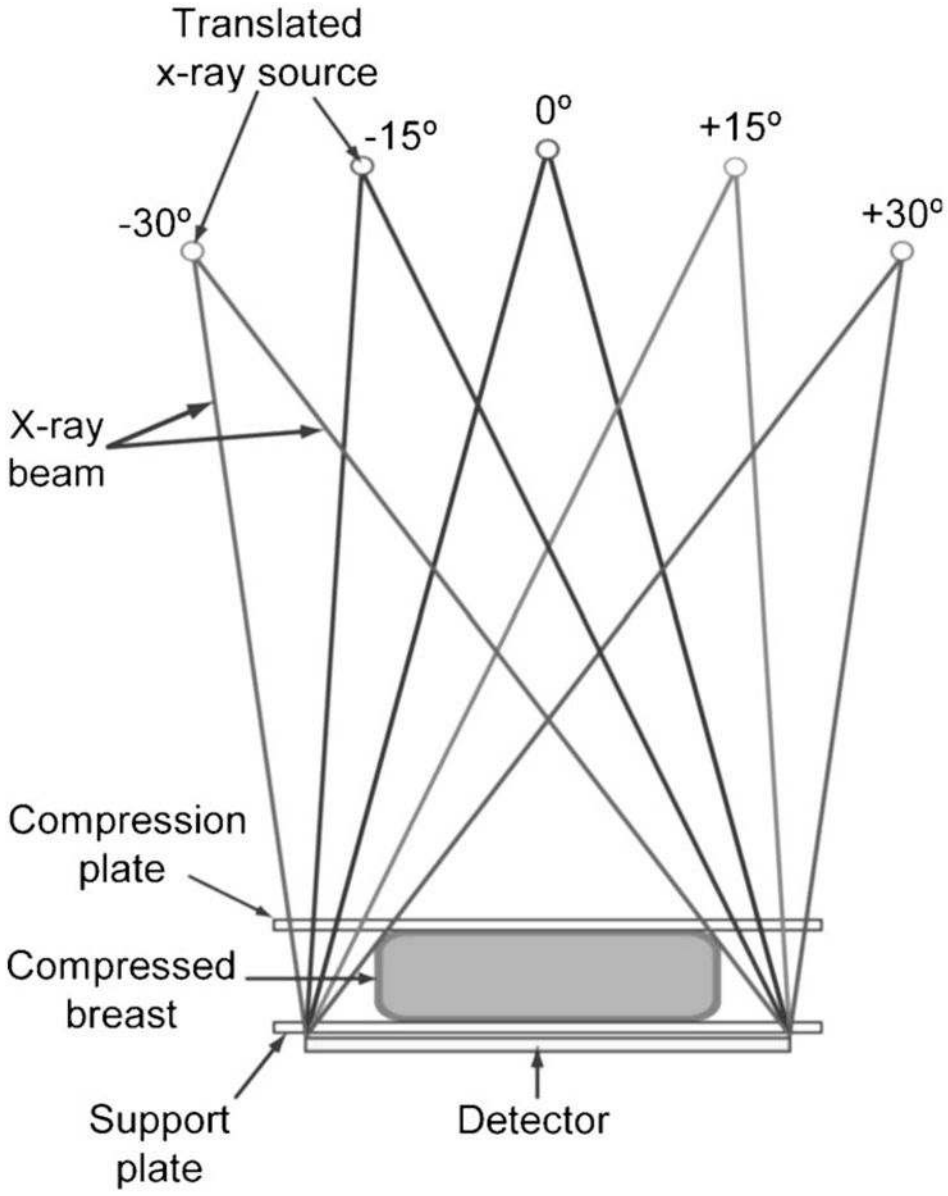

Fig. 1.
Diagram of a tomosynthesis acquisition depicting the moving x-ray source and the stationary detector.

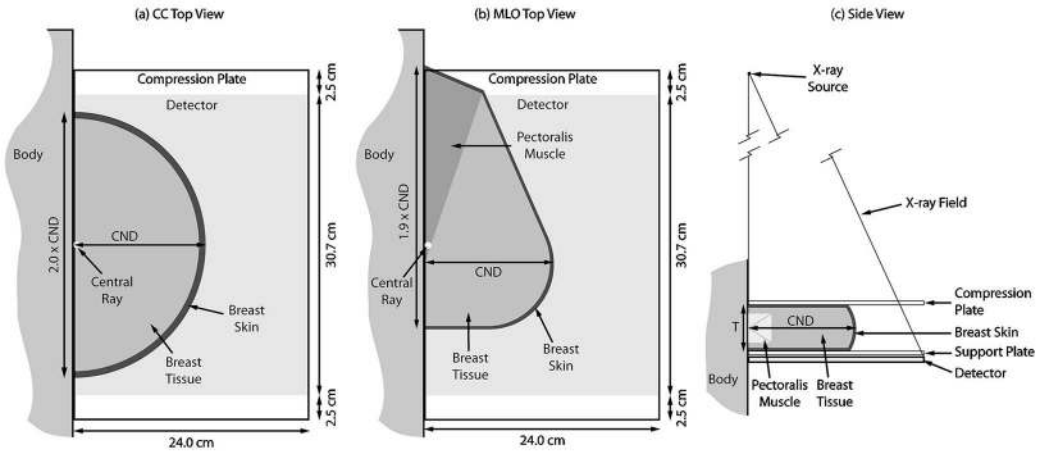

Fig. 2.

Diagram of the simulated CC and MLO views: (a) CC top view, (b) MLO top view, and (c) side view (in the CC view breast, the pectoralis muscle is not present). The pectoralis muscle's thickness decreases towards the caudal side.

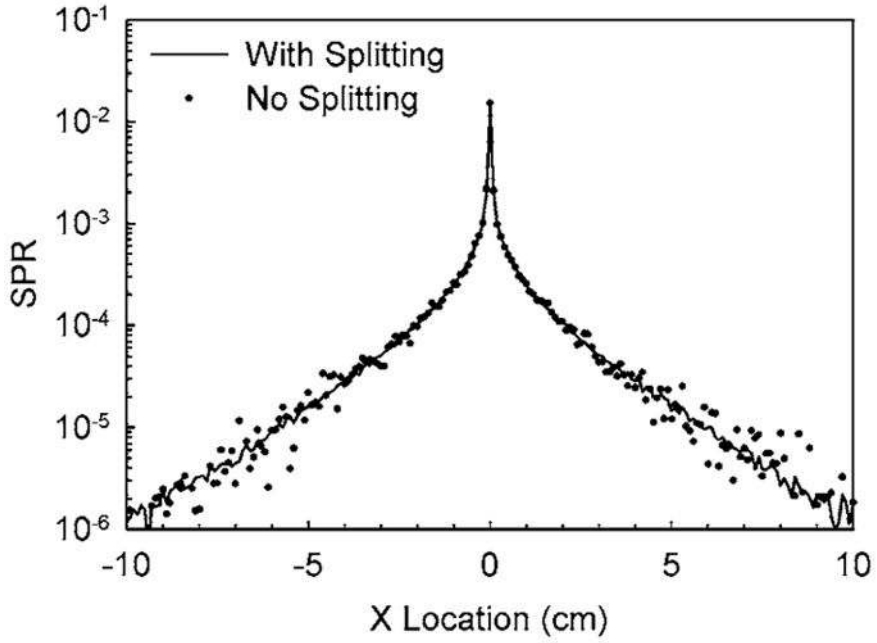

Fig. 3.

Comparison of a scatter PSF computed with and without the variance reduction scheme. The validity of the results computed with the variance reduction scheme is apparent.

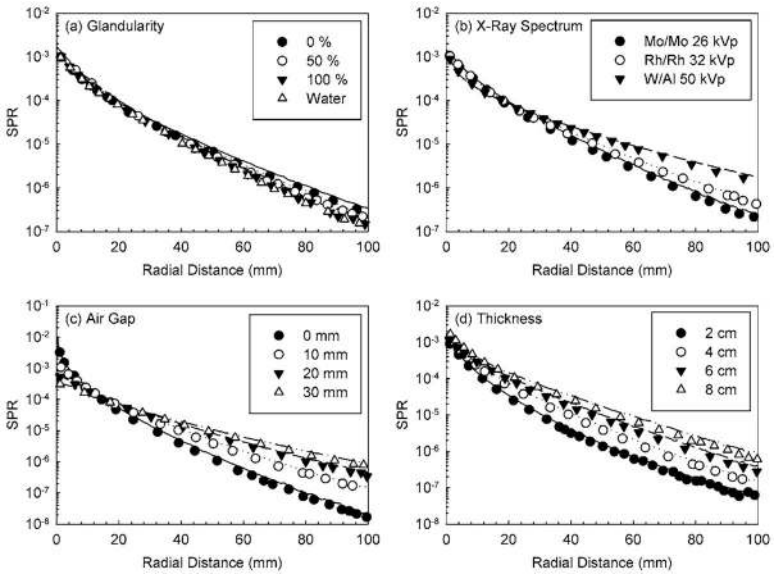

Fig. 4.

Comparison of the scatter PSF computed by the Geant4 program (lines) against those previously reported by Boone and Cooper (symbols) (Ref. 24). Excellent agreement can be seen for all cases.

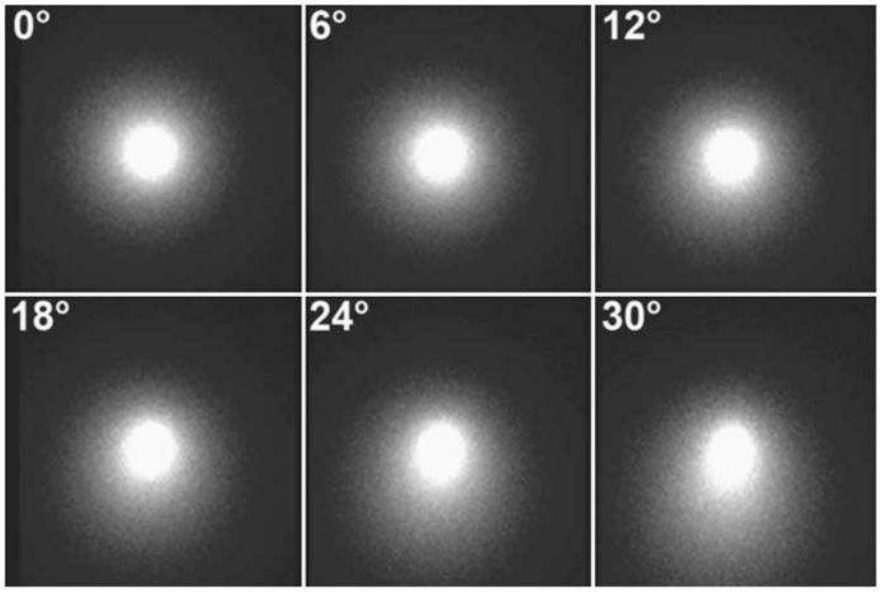

Fig. 5.

Images of the scatter PSF for a 5 cm compressed breast in the CC view for projection angles from 0° to 30°, in 6° steps. The loss of circular symmetry with increasing projection angle is apparent. The x-ray tube moves towards the top of the page with increasing projection angle.

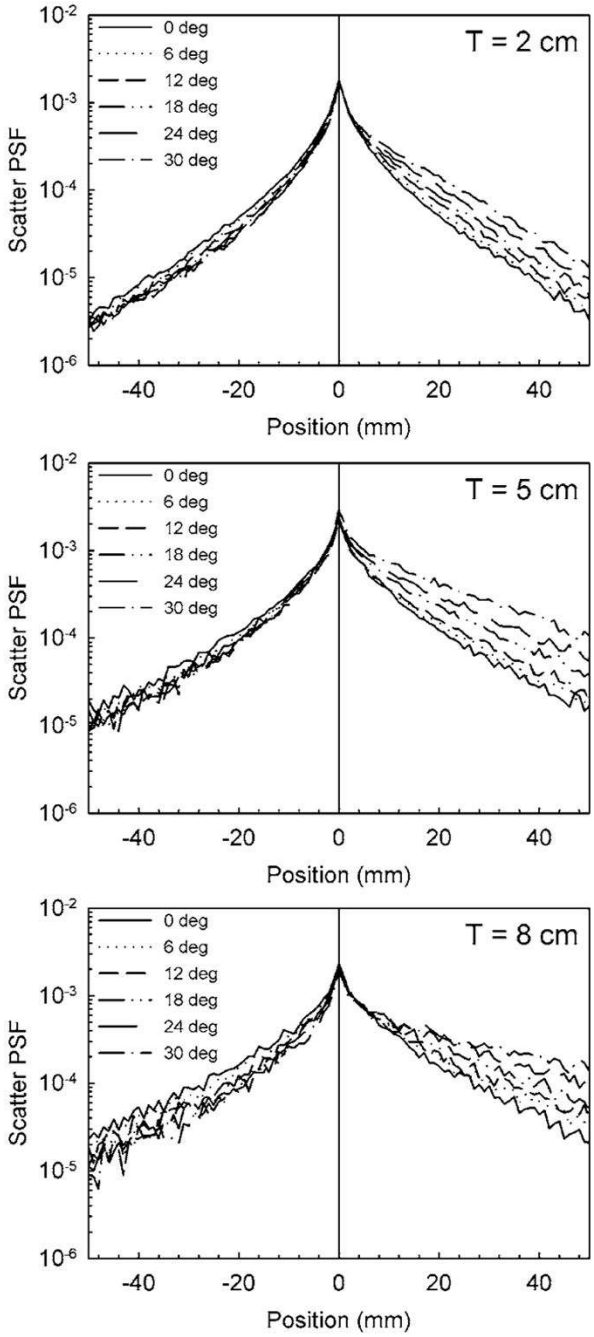

Fig. 6.

Vertical profile through the center of the scatter PSF of breasts of thickness 2, 5, and 8 cm. The loss of symmetry with increasing projection angle is apparent.

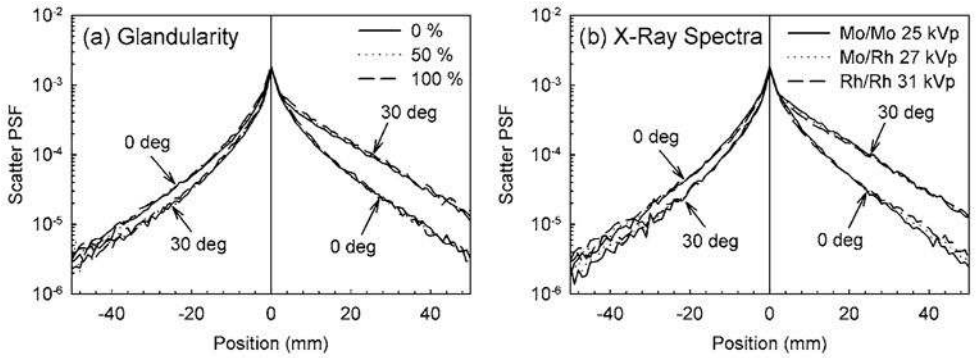

Fig. 7.

Sample graphs showing the variation of the 0° and 30° scatter PSF with varying (a) breast glandular fraction and (b) x-ray spectrum. Both graphs are for a breast with CND =11.6 cm, *T*=5 cm, *G*=50%, and Rh/Rh 31 kVp x-ray spectrum, unless specified otherwise.

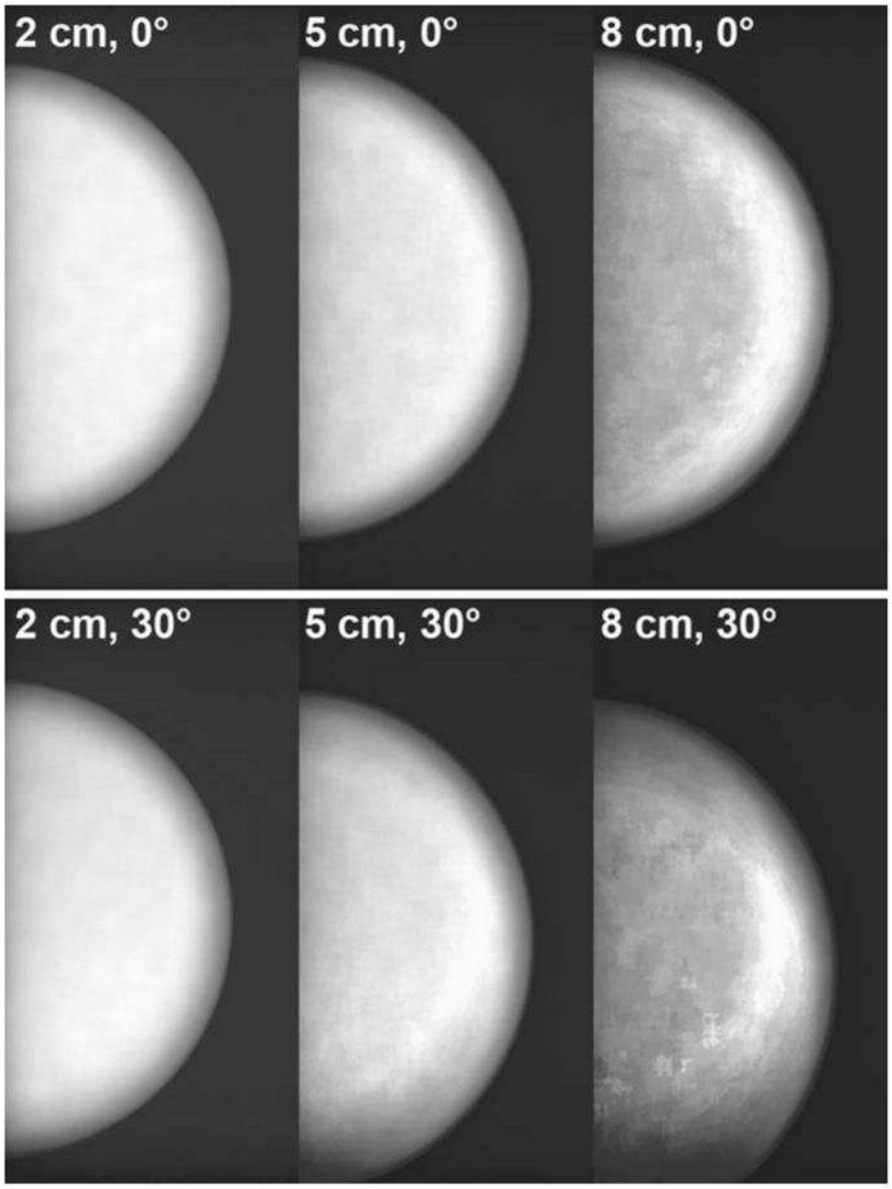

Fig. 8.

Images of the SPR for a CC view breast showing the effect of the breast support plate and the detector cover plate. The increases in SPR near the edges of the breast for the 5 and 8 cm thick breast are apparent for both the 0° and the 30° projections. The breast has a CND=11.6 cm, *G*=50%, and the x-ray spectrum is Rh/Rh 31 kVp.

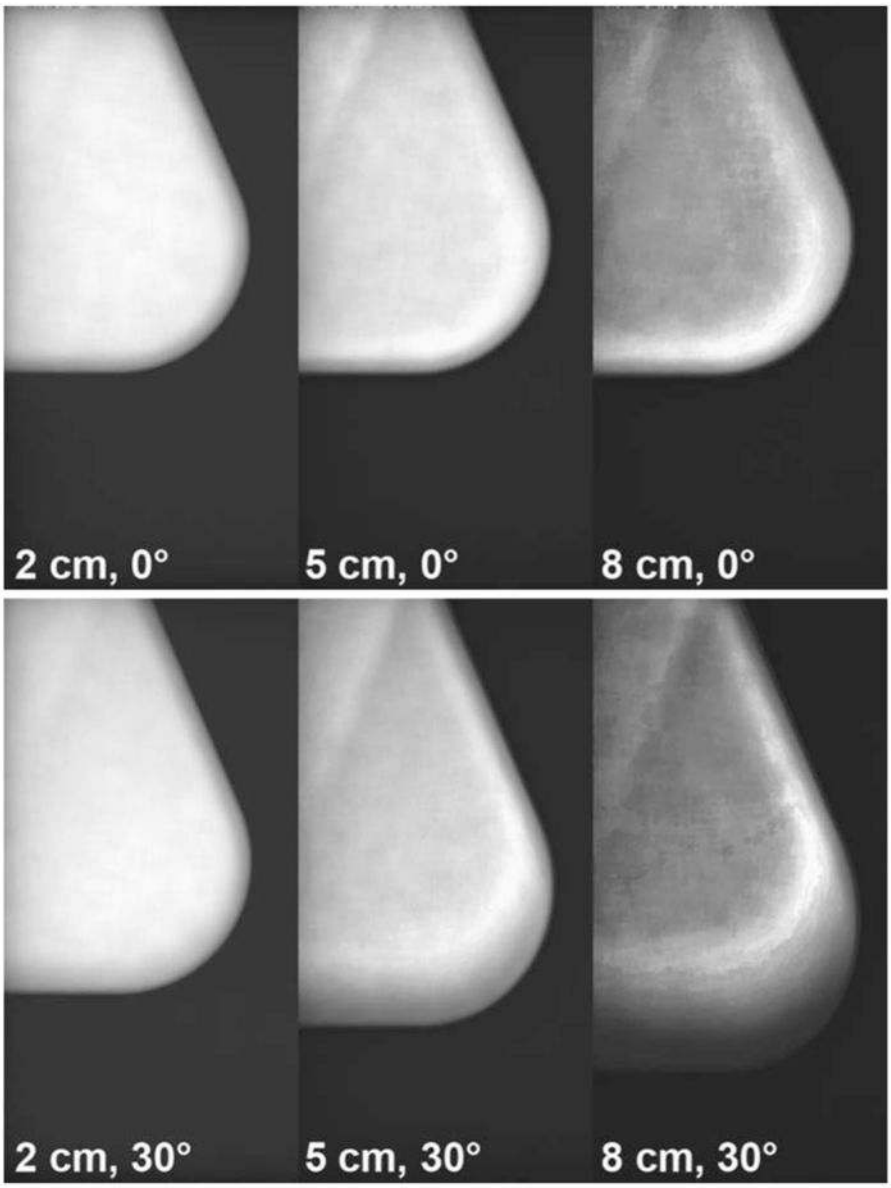

Fig. 9.

Images of the SPR for a MLO view breast showing the effect of the breast support plate and the detector cover plate. The increases in SPR near the edges of the breast for the 5 and 8 cm thick breast are apparent for both the 0° and the 30° projections. The breast has a CND=11.6 cm, *G*=50%, and the x-ray spectrum is Rh/Rh 31 kVp.

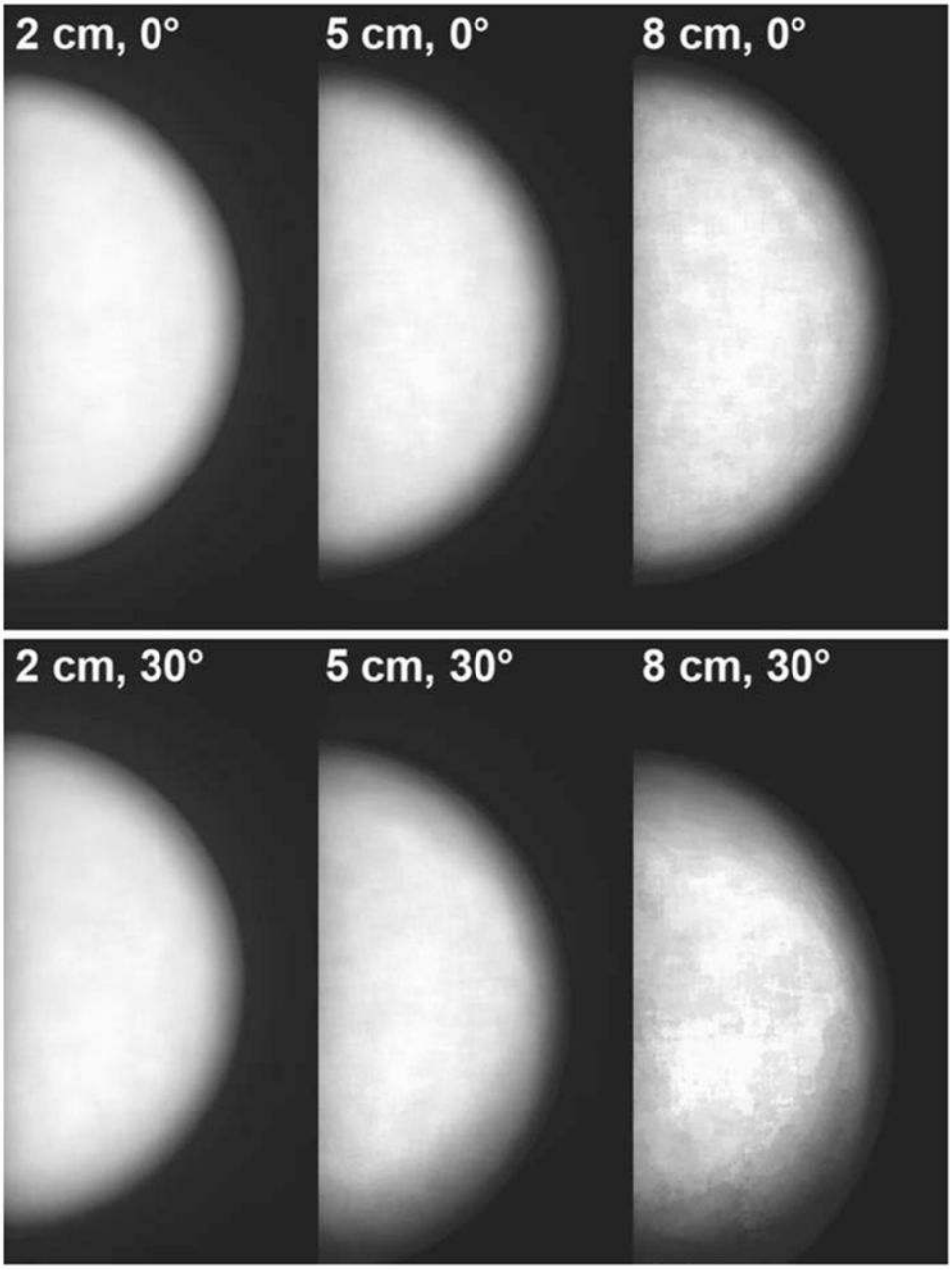

Fig. 10.

Images of the SPR for a CC view breast showing the absence of the increase in SPR when the breast support plate and the detector cover plate are not present. The simulation parameters are the same as those depicted in Fig. 8.

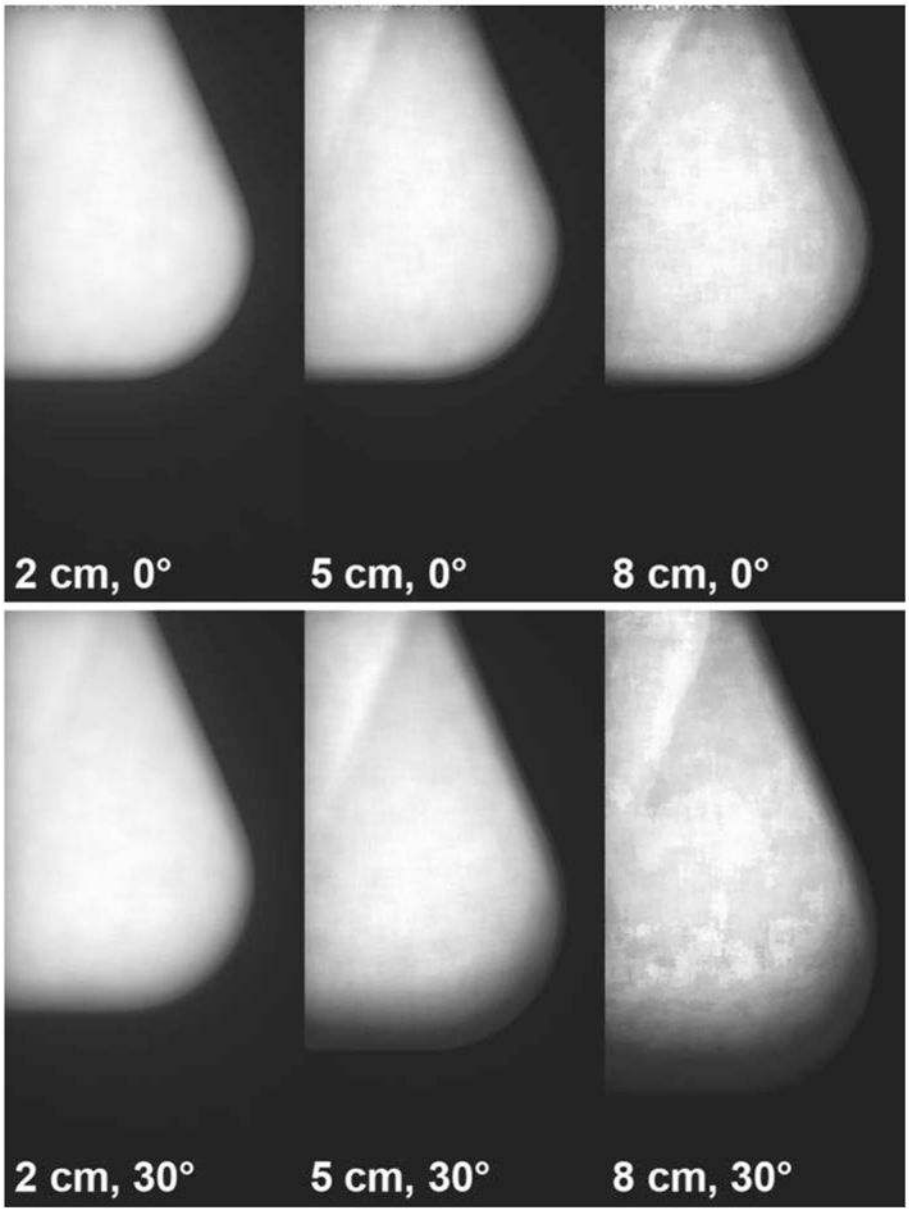

Fig. 11.

Images of the SPR for a MLO view breast showing the absence of the increase in SPR when the breast support plate and the detector cover plate are not present. The simulation parameters are the same as those depicted in Fig. 9.

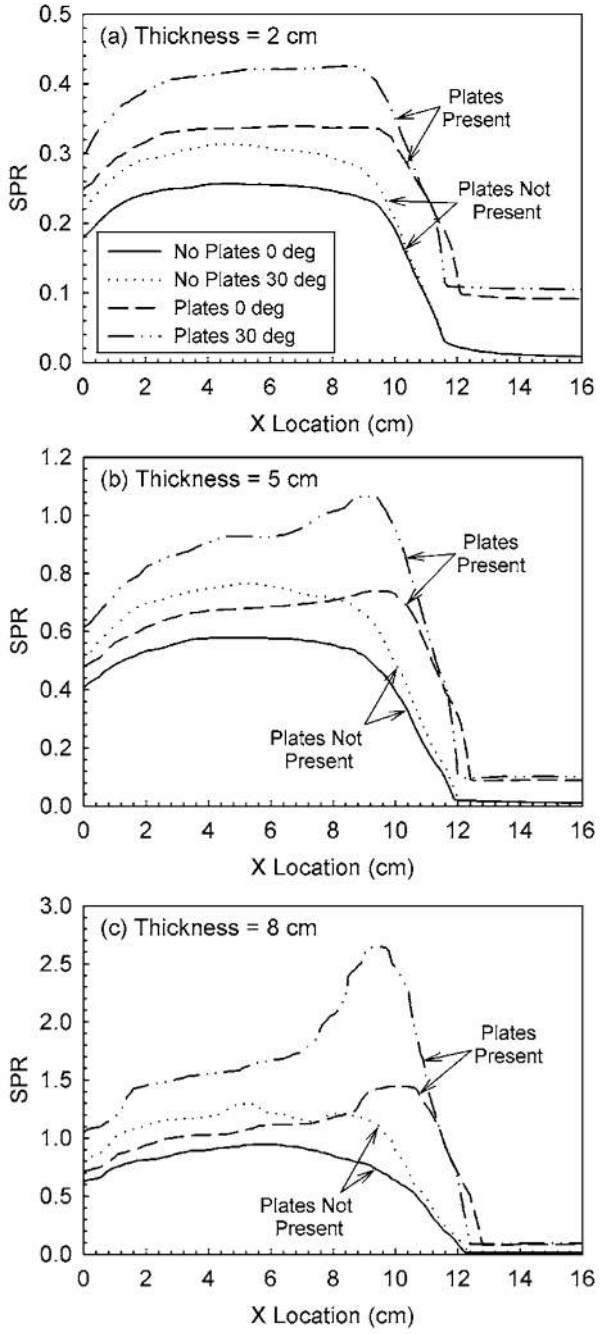

Fig. 12.

Horizontal profiles through the center of mass of the breast of the SPR maps depicted in Figs. 8 and 10.

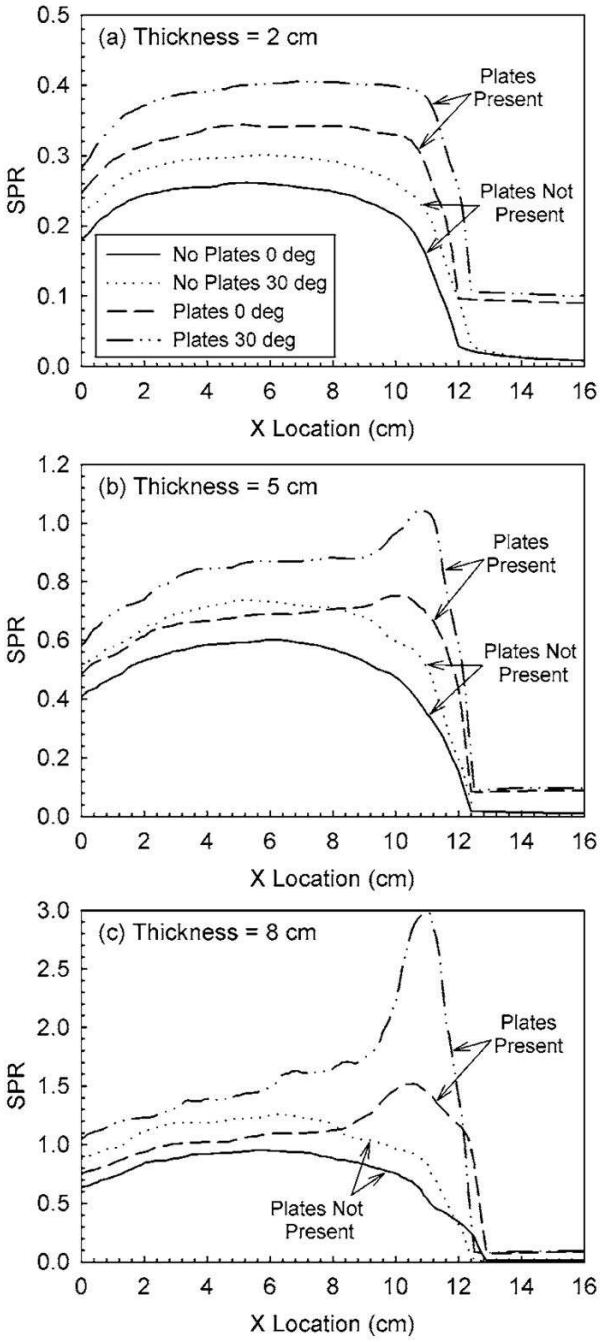

Fig. 13.

Horizontal profiles through the center of mass of the breast of the SPR maps depicted in Figs. 9 and 11.

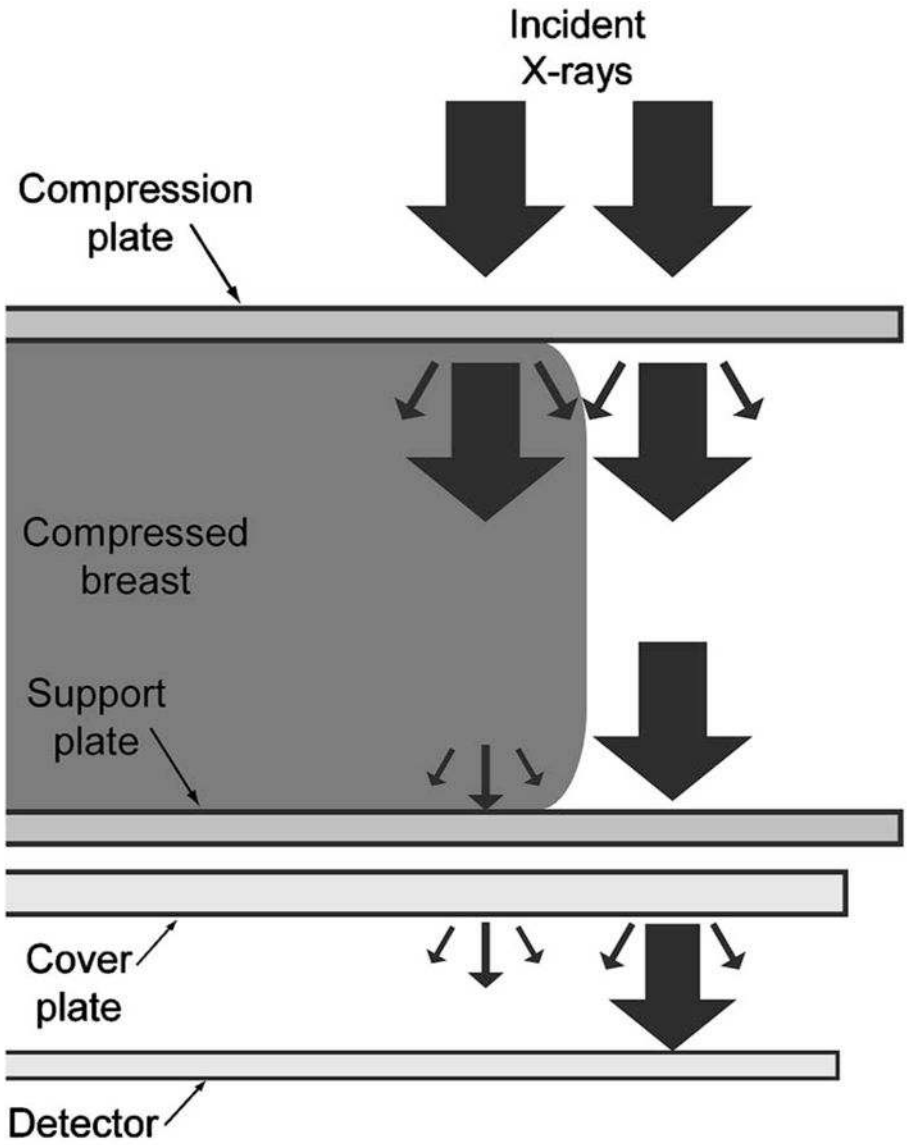

Fig. 14.

Diagram showing the cause of the SPR increase due to the presence of the breast support plate and the detector cover plate. The straight downward arrows depict the primary x rays. The diagonal arrows depict the scattered x rays. Although the plates are very thin, the much higher x ray fluence entering the breast support plate results in a considerable amount of scattered x rays. The portion of these x rays that is detected under the shadow of the breast is divided by the much lower number of primary x rays that travel through the breast, resulting in a high scatter to primary ratio.

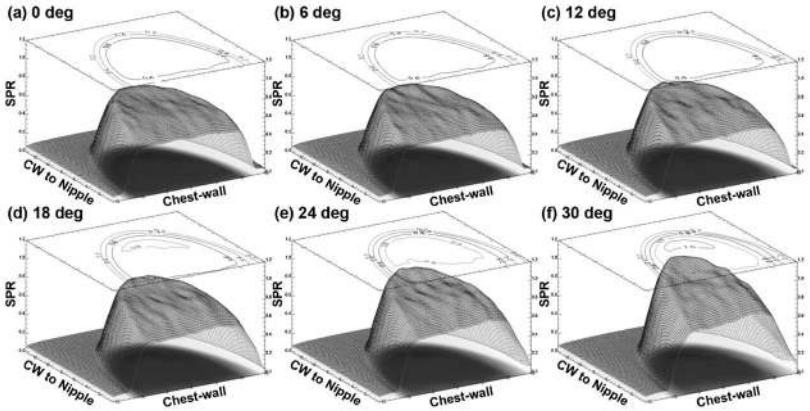

Fig. 15.

Surface and contour plots of the SPR for a CC view breast with CND=11.6 cm, *T*=5 cm, *G*=50%, and projection angles 0° to 30° in 6° steps. The spectrum is Rh/Rh 31 kVp. The increase in SPR, widening tail, and loss of symmetry with increasing projection angle is apparent. The x-ray tube's motion is towards the negative side with increasing projection angle.

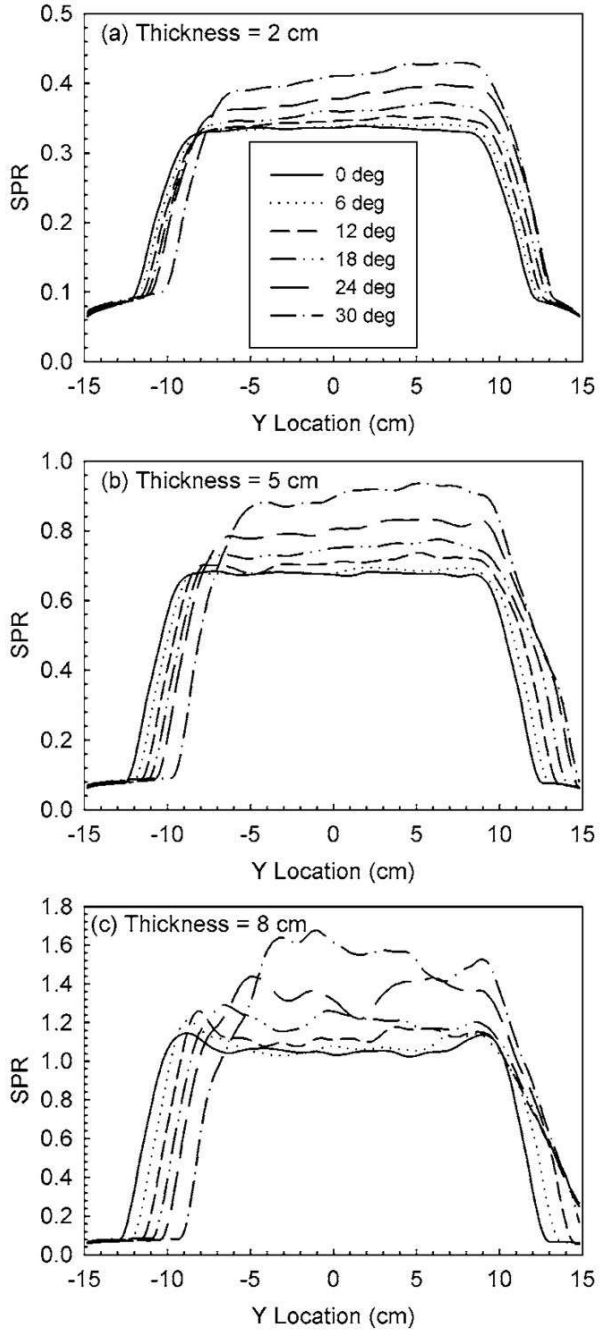

Fig. 16.

Profiles parallel to the chest-wall, through the center of mass, of the CC view breast with a thickness of 2, 5, and 8 cm.

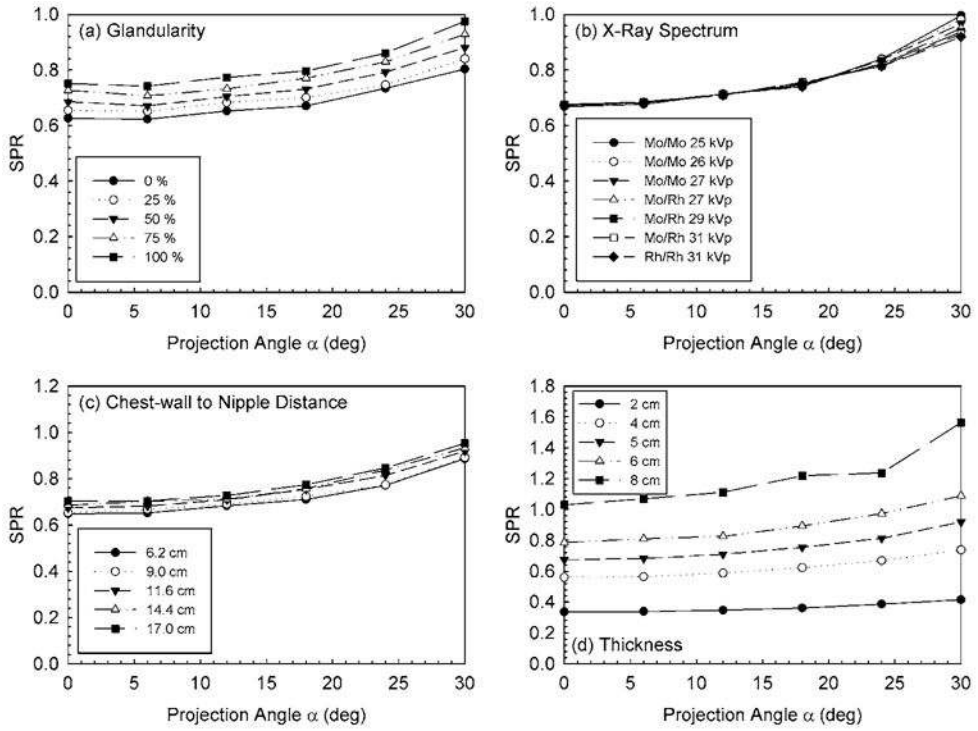

Fig. 17.

Sample graphs of SPR variation with varying (a) breast glandular fraction, (b) x-ray spectrum, (c) chest wall to nipple distance, and (d) compressed breast thickness. All four graphs are for CC view, CND =11.6 cm, *T*=5 cm, *G*=50%, and Rh/Rh 31 kVp x-ray spectrum, unless specified otherwise.

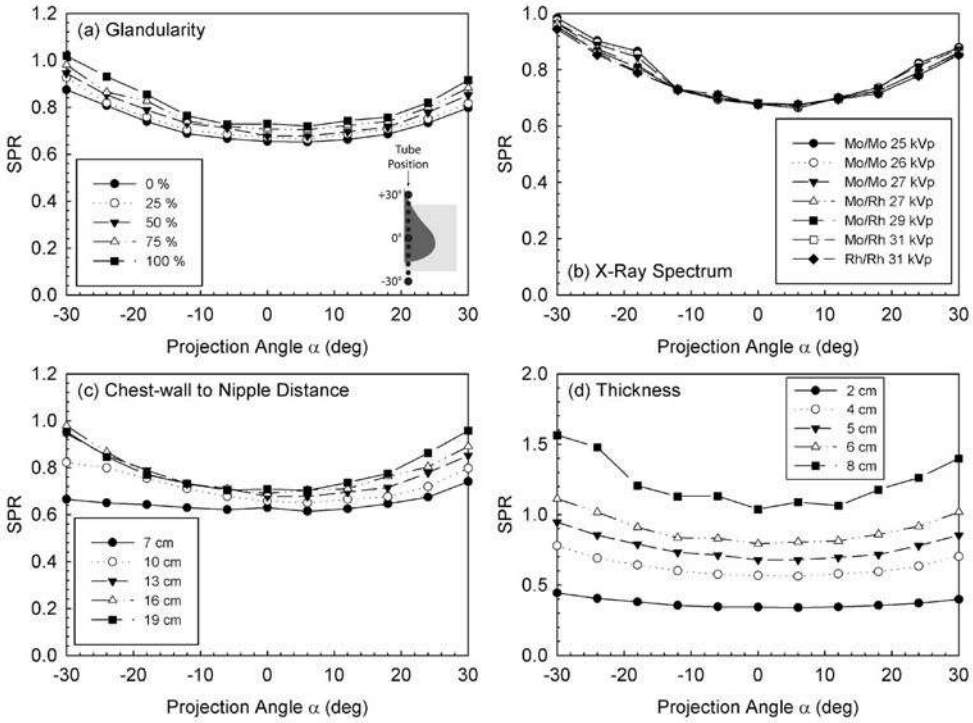

Fig. 18.

Sample graphs of SPR variation with varying (a) breast glandular fraction, (b) x-ray spectrum, (c) chest wall to nipple distance, and (d) compressed breast thickness. All four graphs are for MLO view, CND =13 cm, *T*=5 cm, *G*=50%, and Rh/Rh 31 kVp x-ray spectrum, unless specified otherwise. Positive angle projections are defined as when the x-ray tube swings towards the cranial side of the patient.

Table I

Values of the geometric parameters used in the Monte Carlo simulations for the scatter to primary ratio studies.

Parameter	CC View	MLO View
Breast size studies		
Chest-wall to nipple distance (CND)	6.2, 9.0, 11.6, 14.4, and 17.0 cm	7, 10, 13, 16, and 19 cm
Thickness (T)	2, 4, 5, 6, and 8 cm	
Glandularity (G)	50%	
Breast Composition Studies		
Chest-wall to nipple distance (CND)	11.6 cm	13 cm
Thickness (T)	2, 5, and 8 cm	
Glandularity (G)	0%, 25%, 50%, 75%, and 100%	

Table II

First half-value layer values of the x-ray spectra used to combine the mono-energetic Monte Carlo results. The mono-energetic results were combined using the computed HVL above the breast compression plate due to the inclusion of the breast compression plate in the simulation.

Target	Filter	Tube potential (kVp)	Computed HVL above compression plate (mm Al)	Computed HVL under compression plate (mm Al)
Mo	Mo	25	0.284	0.322
Mo	Mo	26	0.297	0.335
Mo	Mo	27	0.309	0.347
Mo	Rh	27	0.364	0.400
Mo	Rh	29	0.387	0.422
Rh	Rh	29	0.380	0.426
Rh	Rh	31	0.408	0.457

Table III

Coefficients for the fit equations (1) and (2) to compute scatter to primary ratios at the center of mass, for both the MLO and CC views.

Coefficients	MLO view	CC view
a	1.324 300 0E-03	2.088 620 0E-03
b	9.337 850 0E-01	8.955 690 0E-01
c	1.169 212 7E-01	9.800 114 0E-02
d	9.455 517 7E-02	1.116 426 5E-01
e	−3.004 900 0E-04	−8.647 030 0E-03
f	−7.611 100 0E-03	1.836 750 0E-04
g	3.920 070 0E-05	6.499 170 0E-05
h	−1.561 400 0E-04	−6.258 962 0E-02
I	−9.134 761 0E-02	−8.497 300 0E-04
j	−6.803 400 0E-04	−1.188 400 0E-04
k	1.499 353 0E-03	−1.570 300 0E-06
l	−1.033 000 0E-04	
m	−7.712 700 0E-06	